Impact of terahertz short pulses on the oxygen defect state in TiO_{2-x}

Paola Di Pietro,[1] Johannes Schmidt,[1] Nidhi Adhlakha,[1,2] Sandeep Kumar Chaluvadi,[3] Federico Mazzola,[3,4] Veronica Stopponi,[3] Luca Tomarchio,[5] Pasquale Orgiani,[3] Stefano Lupi,[3] and Andrea Perucchi[1]

[1]*Elettra - Sincrotrone Trieste S.C.p.A, S.S. 14 km163.5 in AREA Science Park, 34012 Trieste, Italy*

[2]*Department of Physics, National Institute of Technology Karnataka, Surathkal, Mangalore, 575 025 Karnataka, India*

[3]*CNR-IOM – Istituto Officina dei Materiali, 34149 Trieste, Italy*

[4]*CNR-SPIN, c/o Complesso di Monte S. Angelo, 80126 Napoli, Italy*

[5]*Dipartimento di Fisica, Università di Roma Sapienza, P.le Aldo Moro 2, 00185 Roma, Italy*

(Received 14 October 2024; accepted 20 February 2025; published 3 April 2025)

Oxygen-deficient titanium dioxide (TiO_{2-x}) is a very attractive material for several applications ranging from photocatalysis to resistive switching. Oxygen vacancies turn insulating anatase titanium dioxide into a polaronic conductor, while creating a defect-state band below the ultraviolet semiconducting gap. Here we employ a combination of broadband infrared (IR) reflectivity and THz-pump/IR-probe measurements to investigate the relationship between localized defect states and delocalized conducting polaronic states. We show that the THz pump allows to convert deeply localized electrons into metastable polarons with a lifetime in the ns range. These long-lived metastable states may find application in novel optoelectronic applications exploiting the interplay of dc resistivity, with terahertz and infrared signals.

DOI: 10.1103/PhysRevResearch.7.023011

I. INTRODUCTION

Titanium dioxide TiO_2 is a largely available, naturally occurring oxide which is being used for many applications since hundreds of years ago. It is chemically inert and semiconducting, and exhibits photocatalytic activity in the presence of light with energy equal to or higher than its electronic band gap [1,2]. Its photocatalytic activity allows for thin coatings exhibiting self-cleaning and disinfecting properties under exposure to ultraviolet radiation. Due to its large (3.2 eV) band gap, TiO_2 is also used as a white pigment for the preparation of enamels, cosmetics, and sunscreens. Exciton dynamics in stoichiometric TiO_2 has been extensively studied with above-gap UV pump-probe technique [3–7]. Nonetheless, for some photocatalytic applications the ultraviolet band gap represents a limiting factor, because of the limited portion of the solar spectrum (5%) exceeding the interband transition threshold [8].

The introduction of oxygen vacancies (V_Os) through annealing procedures brings in very important changes to the electrodynamic properties of TiO_2. The onset of a sizable Drude conducting term is accompanied by the appearance of infrared absorption bands [9]. While those terms originate all from the oxygen defects, it is far from obvious whether they belong to the same type of V_O. Angle-resolved photoemission together with DFT (density-functional theory) calculations suggest, on the contrary, the coexistence of distinct localized and delocalized states, with different spatial location and diffusion kinetics [10,11].

Oxygen vacancies in TiO_{2-x} are being studied extensively due to their ability to enhance the photocatalytic activity of TiO_{2-x}, which is important for various applications such as photocatalytic degradation of pollutants and water splitting for hydrogen production. V_Os also play a prominent role in the engineering of resistive-switching properties, thereby allowing the use of TiO_{2-x} as a memristor [12–16] for in-memory computing schemes.

We employ here a subgap terahertz (THz) excitation to achieve control on the oxygen-defect state, thereby modulating the infrared response associated to the photoexcitation of V_Os [see Figs. 1(a), 1(b)]. Our work highlights the presence of very different relaxation dynamics. A fast response (sub-ps) closely follows the THz excitation, after which a very long (ns) relaxation dynamics takes place, associated to the formation of a metastable state. The dynamics unveiled by our THz-pump/IR-probe experiment allows to interpret this transient state in terms of a conversion from deep localized defect states to delocalized large polarons, and back [17,18]. This finding has important consequences towards the exploitation of TiO_{2-x} for solar-energy conversion, as well as in novel optoelectronic applications, for instance designing memristors realizing high-bandwidth neuromorphic vision [19,20].

II. STEADY-STATE CHARACTERIZATION

Very high crystalline quality of anatase TiO_{2-x} thin films of 40 nm thick were deposited on double-sided polished $LaAlO_3$ (001) substrates by pulsed laser deposition (PLD) technique (see Appendix A). In this study, three samples—as-grown (S1), 30 minutes (S2), and 60 minutes (S3)—UHV

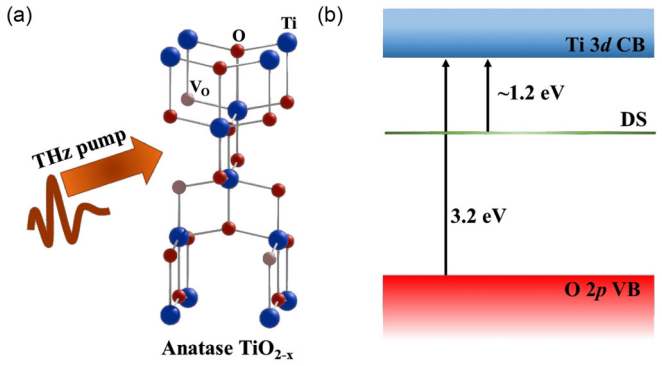

FIG. 1. (a) Crystal structure of anatase TiO_{2-x}. (b) Schematic distribution of the electronic bands in oxygen deficient TiO_2, where DS indicates the defect state.

(ultrahigh vacuum) postannealed films were chosen [9,21]. The crystalline quality of the films was measured by an x-ray diffractometer as shown in Fig. 2. The $\theta - 2\theta$ XRD of the as-grown film shows Laue oscillations indicating very high crystalline quality of the film. For the UHV postannealing samples, two features were observed: (i) Laue oscillations tend to disappear owing to increase in structural disorder, and (ii) red shift in the 2θ peak position of the (004) A-TiO_2 (inset of Fig. 2 corresponding to the expansion of out-of-plane lattice constant "c," i.e., increase in oxygen vacancies in the film [9]). Broadband optical reflectivity measurements have been performed from the THz (3 THz ~12 meV) to the ultraviolet (~6.5 eV) spectral range on S1, S2, and S3 samples. Reflectivity measurements at nearly normal incidence up to 1 eV were performed with a Bruker spectrometer at the SISSI-Mat beamline of the Elettra storage ring [22], by employing different combinations of beam splitters and detectors. Above this frequency, in the visible and ultraviolet spectral range up

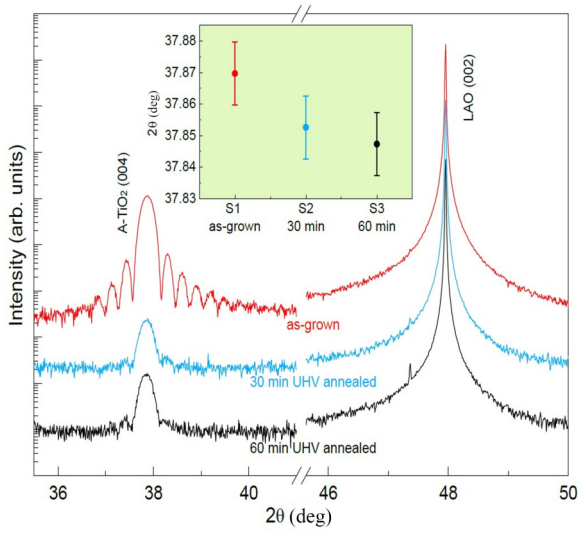

FIG. 2. $\theta - 2\theta$ symmetrical XRD scans of anatase TiO_{2-x} thin films deposited on $LaAlO_3$ (substrates) under different postannealing conditions, respectively. Inset shows the (004) A-TiO_2 peak position of three different films.

to 6.5 eV, data were acquired with a Jasco V730 spectrometer at the "Sapienza" University of Rome.

In the far-infrared range, i.e., below ~0.1 eV, the reflectivity is dominated by the infrared phonon modes (Reststrahlen bands) of the $LaAlO_3$ substrate, which are only partially screened by the thin TiO_{2-x} film [Fig. 3(a)]. The more conducting is the film, the lower is the reflectivity of the Reststrahlen band components. At higher frequencies, the enhancement of the sample reflectivity with respect to that of the substrate reflects the onset of absorption bands. In particular, a clear feature peaked at about 1 eV is present in the reflectivity of sample S2. At even higher frequencies, the reflectivity exhibits other peaks, associated to the electronic structure of both the samples and the substrate.

The reflectivity data are fitted within a Drude-Lorentz model [23] describing the complex dielectric function $\tilde{\epsilon}(\omega)$ in the form

$$\tilde{\epsilon}(\omega) = 1 - \frac{\omega_p^2}{\omega^2 + i\omega/\tau} + \sum_{i=1}^{6} \frac{A_i^2}{\left(\omega_{0,i}^2 - \omega^2\right) - i\omega/\tau_i}. \quad (1)$$

Here, ω_p is the Drude plasma frequency (ω_p^2 is the Drude spectral weight), while A_i represent the oscillator strengths of the minimal set of six Lorentzian components necessary to reproduce our data. Two Lorentzian oscillators are employed for intragap bands: one midinfrared (MIR) band and one near-infrared band. The remaining four oscillators describe ultraviolet intergap bands. The fitting formula takes into account the reflection from both the thin film and the substrate within the Fresnel formalism, as already done in Ref. [9] (see also Appendix B). For all samples the optical conductivity above 3.2 eV suddenly increases as a consequence of the onset of the electronic band gap [see Fig. 3(b)]. On the low-frequency side, one can clearly distinguish the presence of an overdamped Drude term in the annealed samples (S2 and S3). The infrared spectral weight is taken into account here by the combination of the MIR and near-infrared components, centered at about 0.5 ($\omega_{0,1}$) and 1.2 eV ($\omega_{0,2}$) respectively. The sum of these two components ($A_1^2 + A_2^2$) is reported in Fig. 3(c), as a function of the Drude spectral weight ω_p^2.

The infrared spectral weight monotonically grows with the increase of the Drude term. By looking more in detail at the fitting components one notices that the MIR band intensity (red dots) reaches its maximum for sample S3, whereas in sample S2 the component providing the largest contribution to the infrared spectral weight is the near-infrared band (blue triangles). It is tempting to interpret this behavior of the optical conductivity within the traditional dichotomy between deep and shallow donors, which is often discussed in TiO_{2-x} literature [24].

The coexistence of a Drude term together with a MIR band is a ubiquitous phenomenon in transition-metal oxides. In a polar lattice as anatase TiO_2 the midinfrared absorption is usually interpreted in terms of polaron formation. Excess electrons delocalized over several Ti atoms interact with O^{2-} ions, thereby inducing a distortion of the lattice, which can be seen as a large polaron [17,18]. In oxygen deficient TiO_2, the infrared spectral signature of the presence of oxygen vacancies is represented by a near-infrared feature accounting for a deep localized electron (usually referred as defect state,

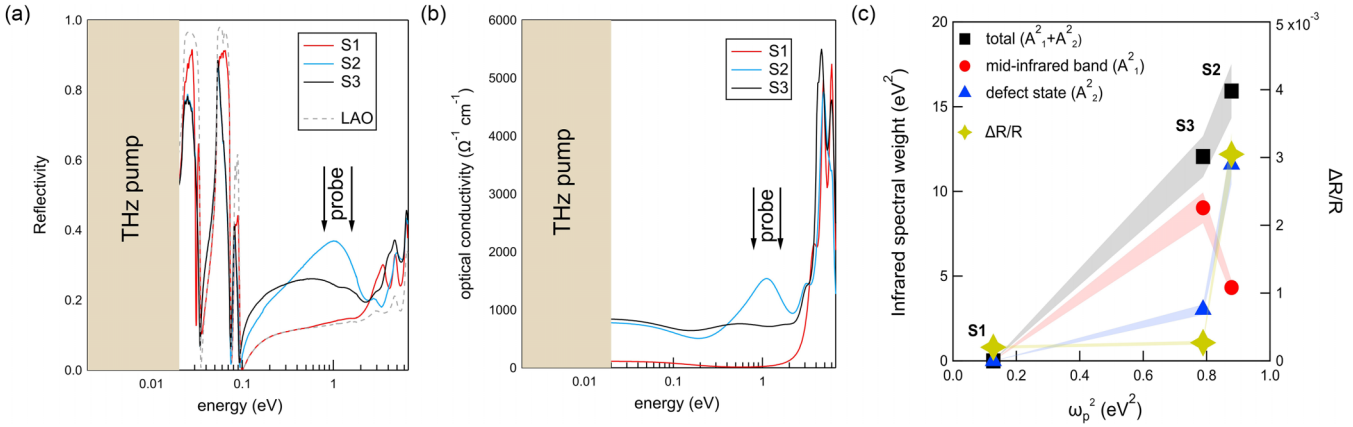

FIG. 3. (a) Optical reflectivity measurements performed on the S1, S2, and S3 TiO_{2-x} thin films, deposited on $LaAlO_3$ (001) substrate. (b) Real part of the optical conductivity, as extracted from a Drude-Lorentz modeling of the data in (a). (c) Spectral weight of the infrared components (A_1^2, A_2^2, and their sum $A_1^2 + A_2^2$) from the Drude-Lorentz fitting (see Appendix B), plotted as a function of the Drude spectral weight ω_p^2. $\Delta R/R$ integrated within the first 30 ps is reported on the right scale. The shadows indicate an error bar of 10%.

DS), trapped in a structural lattice distortion induced by the vacancy.

Samples S2 and S3 display a very different distribution of spectral weight between the midinfrared and near-infrared bands. Nonetheless their total infrared spectral weight ($A_1^2 + A_2^2$) is similar, consistent with the fact that the two annealed samples contain similar amount of V_Os, as measured by XRD (see inset in Fig. 2).

To corroborate our attribution and in order to better understand the behavior of the electrons surrounding the oxygen vacancy, we address time-resolved THz-pump/IR-probe spectroscopy. This technique allows exciting electrons localized at the oxygen vacancy by probing the variation of the sample reflectivity at frequencies corresponding to the midinfrared and defect-state excitations.

III. TIME-RESOLVED SPECTROSCOPY

THz-pump/IR-probe measurements have been performed at the TeraFERMI beamline [25,26] of the FERMI facility. TeraFERMI provides broadband (0.3 to 5 THz), short ($\sim 10^2$ fs) and very intense (electric field up to 5 MV/cm) single-cycle pulses to be used as pump beam. The beamline operates by utilizing relativistic subpicosecond electron bunches to emit THz light through coherent transition radiation (CTR). The IR probe pulses are provided by an optically synchronized fiber laser (Menlo C-Fiber 14) within 66 fs jitter [27] with the terahertz radiation. The laser can be employed both at its 1560 nm (0.8 eV) fundamental wavelength or at its second harmonic 780 nm (1.6 eV). A sketch of the setup is shown in Fig. 4(a).

The transient reflectivities of the S1, S2, and S3 samples, measured with the 780 nm probe, are shown in Fig. 4(b) in a time range of 30 ps. The highest response is given by the sample S2, where the static reflectivity at 1.6 eV is the highest [see Fig. 3(a)], while the S1 and S3 samples provide comparable responses. We compare in Fig. 3(c) the area of the $\Delta R/R$ transient response (integrated over the time interval 0–30 ps), with the spectral weight of the various components. It clearly turns out that $\Delta R/R$ directly scales with the intensity of the defect-state component, whereas all other fitting components follow distinctly different behaviours. This confirms that the 780 nm probe measurement explores the dynamics of the defect state after THz photoexcitation. Indeed, since the Drude spectral weight is also not scaling linearly with $\Delta R/R$, we can safely rule out a prominent contribution from free charge carriers to the pump-probe signal.

The THz-pump/780 nm-probe data, shown in Figs. 4(b), 4(c), exhibit the presence of at least three different time scales. A first one is associated to the excitation from the THz pulse, while two very different timescales for relaxation are present. The rise time after photoexcitation is very sharp for all samples. A sigmoidal fit of this feature provides values $\leqslant$100 fs, which corresponds to the rise time of the THz-pump electric field, measured separately by electro-optic sampling (EOS). Within the same time scale is the pulse width of IR probe pulses, here 110 fs, which determines the time resolution of our experiment. One can safely assume that the electronic excitation process takes place in time scale shorter than 100 fs for all samples. The relaxation processes occurring after photoexcitation are being fitted by a standard double-exponential model. The short relaxation (τ_{short}) corresponds to 200, 400, and 260 fs for samples S1, S2, and S3, respectively. It is worth mentioning that for all samples, the relaxation τ_{short} is longer than the decay of the (almost) symmetric single-cycle THz-pump pulse. This is better seen in the inset of Fig. 4(b), comparing the pump-probe signal of sample S2, with the THz electric field. Here, one may notice that while the rise of the $\Delta R/R$ signal matches the rise of the THz pulse, $\Delta R/R$ decays more slowly than the THz electric field. After this first sharp decay, the $\Delta R/R$ becomes almost flat for all samples. If measured over a much longer ($\sim$100 ps) time delay as shown in Fig. 4(c), one can distinguish a long relaxation (τ_{long}) assuming values in the order of ns.

The transient reflectivity of sample S2 has also been measured by employing a 1560 nm probe, in order to investigate the dynamics at a wavelength falling in the spectral region between A_1 and A_2 bands. The response has a positive sign

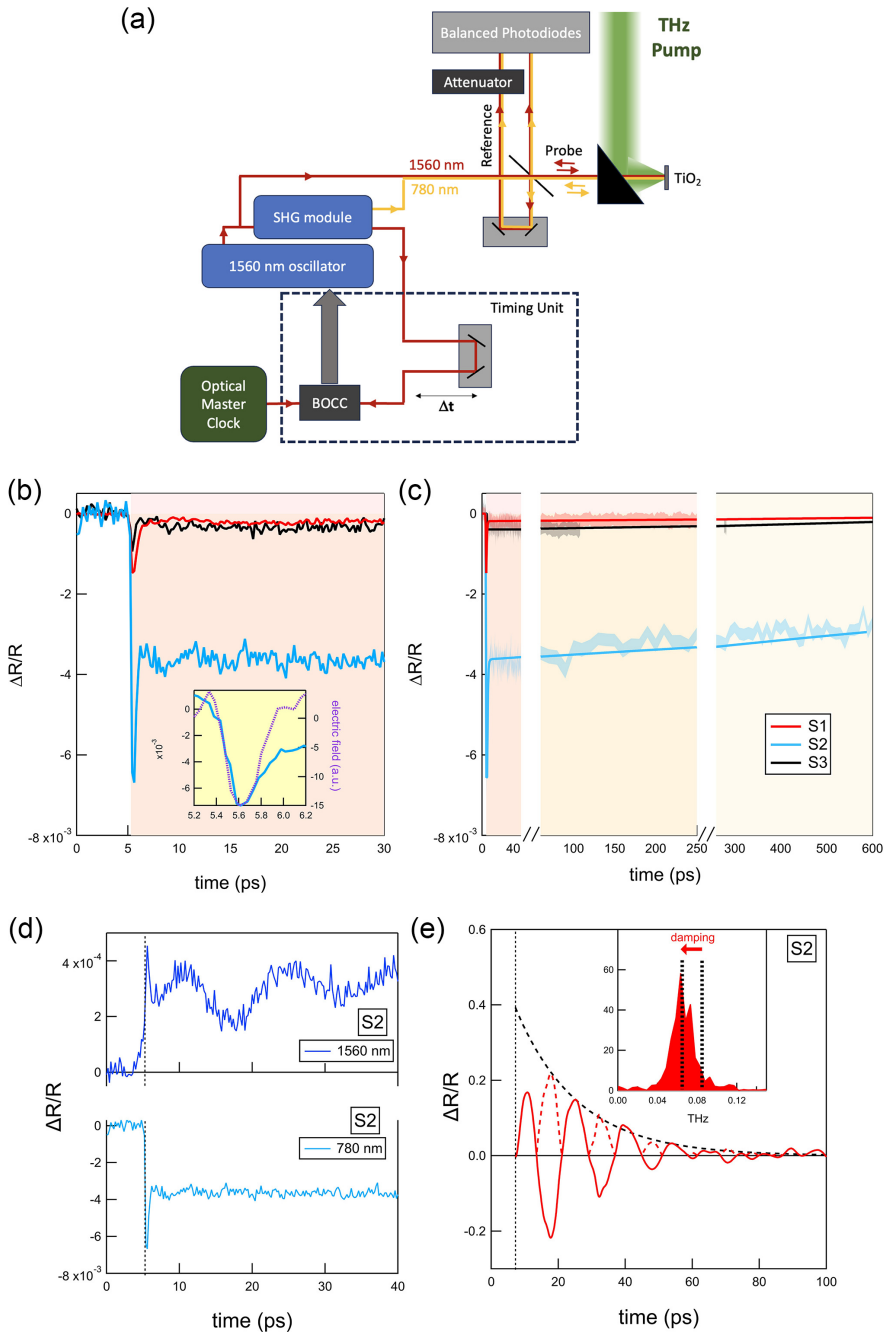

FIG. 4. (a) Sketch of the TeraFERMI THz-pump/IR-probe setup. The strong electric-field THz-pump pulses are provided by the FERMI accelerator facility [25,26]. The probe pulses originate from a Menlo mode-locked fiber-laser oscillator at the fundamental wavelength of 1560 nm. A portion of the pulse coming from the oscillator is used for synchronization with the optical signal from the FERMI master clock, thanks to a balanced optical cross correlator (BOCC). The timing unit includes a delay line allowing to shift the phase (here the THz-pump/IR-probe delay) of the laser pulses with respect to the master clock, through the synchronization loop (see Ref. [28]). The probe pulses are either used at 1560 nm or converted to 780 nm by a second harmonic generation (SHG) module. In the pump/probe setup, a beam splitter is used to pick up a portion of the probe pulse utilized as a reference, while the transmitted portion is incident on the sample, backreflected and picked up by the same beam splitter and steered as a signal to the balanced photodetector. An attenuator and a manual delay line are matching the incoming intensity and the path length of the reference beam, respectively. (b) Transient reflectivity $\Delta R/R$ measured at 780 nm, with a THz pump field of 5 MV/cm in the first 25 ps after the pump arrival, and (c) results with delays up to 600 ps. The inset in panel (b) shows a comparison of the THz pump field (dashed purple line) and $\Delta R/R$ of sample S2 over a short time range. In panel (c) continuous lines are fits to the experimental data which are shown here in shaded colors. (d) Transient reflectivity $\Delta R/R$ measured on sample S2 at 1560 nm, with a THz pump field of 1.25 MV/cm (top panel). $\Delta R/R$ measured at 780 nm ($E_{THz} = 5$ MV/cm, see Appendix C) is also shown for comparison (bottom panel). (e) Oscillations extracted from the curve reported in (d) (top panel), as described in Appendix C. The dashed black line represents the exponential envelope of the damped oscillations. The inset shows the Fourier transform of the oscillations affected by the damping constant, which causes a red shift of the resonance frequency from $f_0 = 85$ GHz to $f_D = 65$ GHz (see main text).

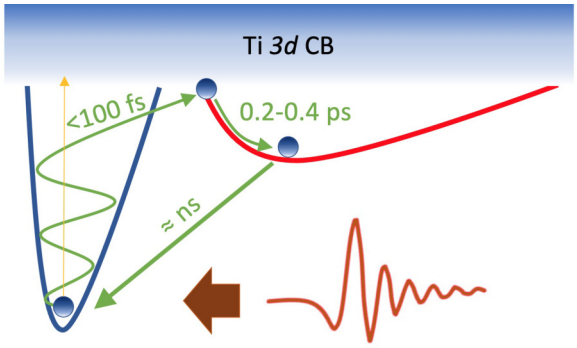

FIG. 5. Sketch of the THz excitation of a deep localized vacancy. The electron localized in the vacancy acquires sufficient energy from the THz field, leading to its photoionization within few 10's fs. A large polaron is then formed within less than 1 ps. This represents a metastable state requiring ∼1 ns before relaxing back to the strongly localized vacancy ground state.

[Fig. 4(d)], contrary to the signal probed at 780 nm. As in the case of the 780 nm measurements, the transient reflectivity includes different dynamical responses, which can be analyzed separately. A first very short and sharp rise is identifiable, after which a long steplike dynamics occurs, with time constant comparable with that found at 780 nm. Moreover, clear oscillations superimpose to the steplike response and are fully damped after ∼50 ps. We will come back to this feature in the next section.

IV. DISCUSSION

The most intuitive interpretation of our experimental data is in terms of polaron excitation by a THz field, as described in the sketch of Fig. 5. The defect state can be seen as a small polaron localized at the oxygen vacancies. The pumping THz field interacts with both the electrons and the ions, thereby providing a displacement strong enough as to climb the defect-state potential well [29], and eventually lead to electrons escape from the oxygen-vacancy site [30]. The photoionized free charge carrier is now allowed to delocalize within the Ti − 3*d* conduction band. The underlying strongly polar lattice leads to large polaron formation, accompanied by a structural distortion extended over several Ti sites. Consistent with previous literature [31], the formation of the polaron occurs between 200 and 400 fs, which is the time interval corresponding to τ_{short}. The large polaron represents a metastable state requiring few ns (τ_{long}) to relax back to the original defect state. This time scale relates to the time needed for a scattering event to take place between the large polaron and an oxygen vacancy, thus allowing the relaxation to the deep defect state to occur.

This polaron interpretation of the THz-pump/IR-probe results is corroborated by an analysis of the sign of the pump-probe signal for the two different probe energies. After the arrival of the THz pump pulse, we expect a drop of the spectral weight associated to the defect state, accompanied by an increase in the midinfrared, large-polaron band. A schematic representation of such scenario is shown in Fig. 6 for sample S2. In Fig. 6 the optical conductivity *before* pump corresponds

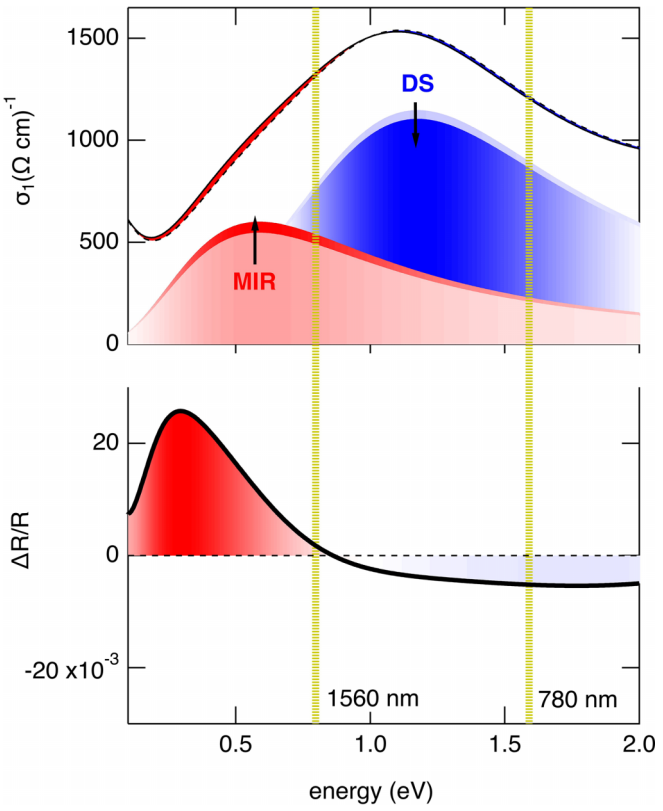

FIG. 6. Variation (colored) of the optical conductivity σ_1 of sample S2 extracted from the FTIR measurement to that simulated *after* a THz pump beam has reduced the spectral weight component A_2 related to the defect state (DS) excitation, while the component A_1 (midinfrared, MIR) simultaneously increases in order to conserve the total spectral weight (top panel). The bottom panel shows the corresponding calculated $\Delta R/R$. The yellow vertical lines indicate the 780 and 1560 nm probe frequencies.

to the one reported in Fig. 3(b), whereas the one *after* pump is a fictitious conductivity constructed by arbitrarily reducing the spectral weight of the defect-state components, while increasing of the same amount the midinfrared band in order to conserve the total spectral weight. A reconstruction of the corresponding transient reflectivities is shown in the lower panel of Fig. 6, thereby highlighting that such a redistribution of the spectral weight induces a reduction of the transient reflectivity at 780 nm, while the transient reflectivity at 1560 nm increases, consistent with the experimental results.

As anticipated in the previous section, the $\Delta R/R$ signal measured at 1560 nm on sample S2 clearly shows the activation of a coherent phonon mode. Following the theory of a damped harmonic oscillator we observe the resonance frequency f_0 of the phonon red shifted by the damping constant $\gamma_D = 1/\tau_D$ in the following way: $f_D = \sqrt{f_0^2 - \gamma_D^2} = 65$ GHz. By reconstructing the exponential envelope of the oscillations [see Fig. 4(e)], we extract a damping constant of $\gamma_D = 54$ GHz and a resonance frequency of $f_0 = 85$ GHz. The damping can be most likely ascribed to the coupling between the phonon and the polaronic charges, due to the interaction among the ions. Indeed, the significant electron-phonon coupling in a polaronic system like TiO_{2-x}, has a crucial role in the transient

atomic vibration of the lattice upon photo-excitation [32]. The inset of Fig. 4(e) shows the Fourier transform of the oscillating curve reported in the main panel (in red). The arrow marks the red shift due to the damping constant. This oscillation frequency $f_0 = 85$ GHz is too low to ascribe it to an optical mode. We therefore attribute it to an acoustic eigenmode of the film.

The frequency of the oscillation f_0 is related to the longitudinal sound velocity v_s, and to the film thickness d through [33]

$$f_0 = v_s/2d. \tag{2}$$

From Eq. (2) we establish $v_s = 6800$ m/s, in agreement with Ref. [34]. With this value of v_s we can use $Z = \rho \cdot v_s$ [35], where $\rho^{TiO_2} = 3900$ kg m^{-3} [36], to estimate the acoustic impedance of the TiO_2 film $Z^{TiO_2} = 2.7 \times 10^{10}$ g m^{-2} s^{-1}. The corresponding impedance for the $LaAlO_3$ substrate [37] is $Z^{LaAlO_3} = 6.5 \times 10^{10}$ g m^{-2} s^{-1}, thus providing an acoustic reflection coefficient $R_{ac} = (Z^{TiO_2} - Z^{LaAlO_3})/(Z^{TiO_2} + Z^{LaAlO_3}) = 0.41$, large enough as to sustain the standing-wave formation. Interestingly, the oscillation is almost absent in the measurement performed with probe wavelength $\lambda = 780$ nm. This important difference between the results obtained at the two wavelengths may be related to the strong coupling between the acoustic phonon and the polaronic midinfrared mode, which is absent in the case of the defect-state contribution. Nonetheless, the larger penetration depth of the 1560 nm probe beam may also play a role in this respect.

V. CONCLUSIONS

We provide here the first time-resolved characterization of oxygen-deficient TiO_2 samples with THz pumping. The comparison between THz-pump/IR-probe measurement and static infrared reflectivity results allows discriminating between deep localized vacancy states and shallow delocalized polaron states. Most interestingly, THz radiation allows converting electrons from the localized state into a metastable large-polaron states, with a ns lifetime. While shedding light on the still controversial physics underlying V_Os state in TiO_{2-x}, our finding has potential implications in novel electro-optic switching devices which combine different ranges of the electromagnetic spectrum. By exploiting its resistive switching properties, as well as its sensitivity to both THz and infrared light, TiO_{2-x} provides the opportunity to combine sensing and processing functions in one single device. Inspired by biological systems, TiO_{2-x}-based neuromorphic devices [19] could process information from a very broad spectral range extending well above and below the visible range, with operation speed in the GHz range.

ACKNOWLEDGMENTS

The authors gratefully acknowledge the FERMI team for their essential support throughout the experiment. A.P. acknowledges G. Perucchi for the artwork in Fig. 1(a).

The authors declare no conflict of interest.

APPENDIX A: SAMPLE PREPARATION AND XRD DETAILS

TiO_2 films were deposited at 720 °C in 10^{-4} mbar oxygen environment and at a substrate-to-target distance of 7 cm, respectively, using the first harmonic of Nd:YAG laser ($\lambda = 1064$ nm) [38,39]. XRD characterization of the films was performed with the X-ray Panalytical Xpert high-resolution diffractometer.

APPENDIX B: STATIC REFLECTIVITY MEASUREMENTS AND ANALYSIS

The reflectivity data have been fitted by the Kramers-Kronig consistent Drude-Lorentz model, which gives the normal-incidence reflectivity of a thin film grown on a substrate when its optical properties are known. This procedure has been addressed by means of the RefFIT software [40]. The fitting procedure considers the thickness of both the film (40 nm in our case) and the substrate (500 μm) to calculate the best reflectivity by optimizing the Drude-Lorentz parameters. Once the best-fitting Drude-Lorentz parameters are obtained, the related dielectric function (and hence the optical conductivity) can be analytically calculated. The data and the related fits are reported in Fig. 7. Table I contains all the Drude-Lorentz parameters used for the three samples.

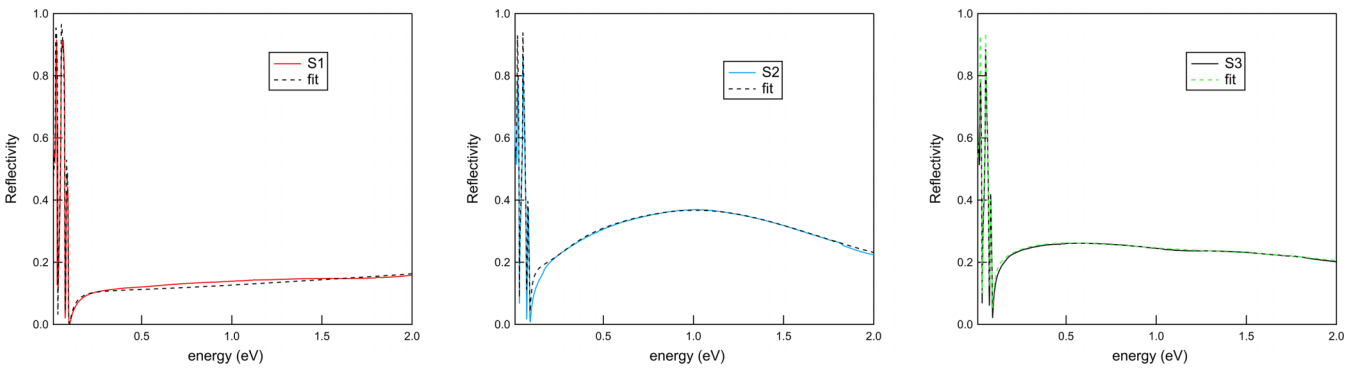

FIG. 7. Reflectivity data of the three samples (S1, S2, and S3) and the corresponding Drude-Lorentz fits.

TABLE I. Drude-Lorentz parameters related to the fits reported in Fig. 7. All numbers (except the ϵ_∞) are in eV.

	S1	S2	S3
ϵ_∞	2.5	2.5	2
ω_p	0.357	0.937	0.888
$1/\tau_{\text{Drude}}$	0.148	0.150	0.124
A_1 (MIR)	–	2.08	3.01
$\omega_{0,1}$	–	0.587	0.574
$1/\tau_1$	–	1.07	1.75
A_2 (DS)	–	3.40	1.74
$\omega_{0,2}$	–	1.18	1.87
$1/\tau_2$	–	1.36	1.67
A_3	3.83	2.68	2.11
$\omega_{0,3}$	3.73	3.04	3.05
$1/\tau_3$	1.15	1.23	0.964
A_4	4.55	6.55	1.99
$\omega_{0,4}$	4.82	4.84	4.13
$1/\tau_4$	0.699	1.35	0.337
A_5	5.76	2.79	6.31
$\omega_{0,5}$	5.99	5.70	4.60
$1/\tau_5$	0.949	0.855	1.16
A_6	–	2.27	5.91
$\omega_{0,6}$	–	6.10	6.01
$1/\tau_6$	–	0.494	1.28

We used one Drude term and six Lorentzian oscillators in total, where A_1 and A_2 indicates the MIR (midinfrared) and DS (Defect State) terms (see main text). The Drude, MIR, and DS bands of the optical conductivities are shown in Fig. 8. The oscillators 3, 4, 5, and 6 are all related to intergap bands (with central frequencies $\omega_0 > 3$ eV). These contributions, i.e., Drude, MIR, DS, and intergap bands, have been already previously used to characterize as-grown and annealed TiO_2 samples in Ref. [9]. In the present case the sample S2 clearly exhibits the most prominent DS band centered between 1 and 2 eV. Nevertheless, a midinfrared band is also necessary to reproduce the observed behavior of the reflectivity. Therefore, we fitted the reflectivity of S2 by employing the aforementioned six Lorentzian oscillators and one Drude term. The same set of components was used to fit the other two samples' reflectivity. We estimate an error bar of about 5% on the fitting parameters provided in Table I, resulting in an error bar of 10% on the spectral weights displayed in Fig. 3(c) of the main text.

APPENDIX C: THZ-PUMP/IR-PROBE MEASUREMENTS

In the experimental setup [see Fig. 4(a)], the THz beam is focused on the sample by a parabolic mirror with a through hole, thus allowing for normal incidence of both pump and probe beams. The THz spot size has been measured by means of a THz camera (Spiricon, Pyrocam IIIHR), resulting in ∼500 μm diameter. The camera has been used to spatially overlap the THz beam and the 780/1560 nm probe beam, which hits the samples by passing through the hole of the parabolic mirror.

THz electric-field time trace has been measured by electro-optic sampling technique. By combining the value of the THz spot size diameter with the THz pulse duration, as extracted by a Gaussian fit of the THz electric field intensity (squared electric-field time trace), the THz electric-field intensity has been retrieved [41]. The difference between the THz electric-field intensities measured at 780 and 1560 nm accounts for different electron-beam conditions in the FERMI accelerator during the two experiments.

The oscillations superimposed to the THz-pump/1560 nm-probe curve are extracted as the difference signal between the measured data and a double-exponential fit. In order to correct for the residual nonlinear pump-probe dynamics, we applied a low-pass filter to determine the baseline and substracted it. As a result, symmetric oscillations with an exponential envelope are retrieved. The curve has been smoothed with a moving-average filter without broadening the oscillation itself.

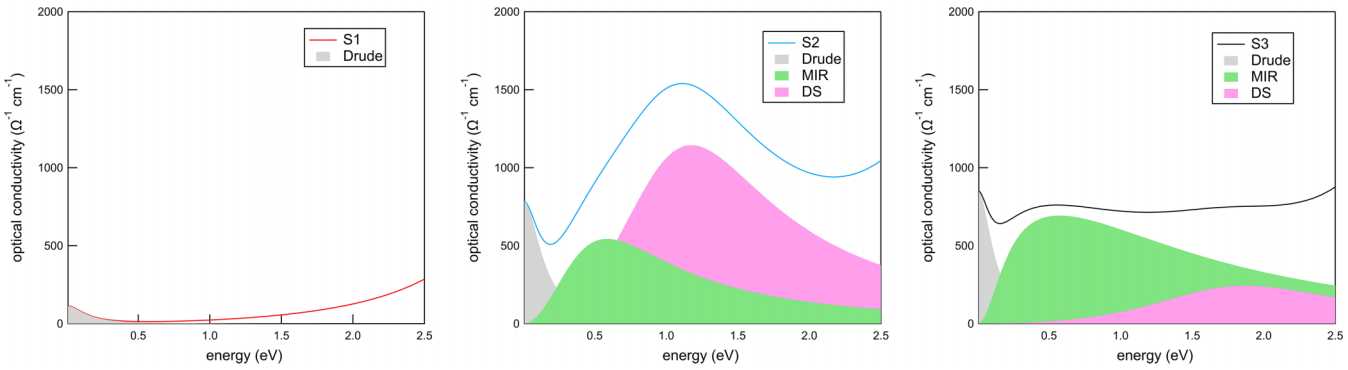

FIG. 8. Optical conductivities for the three samples together with the Lorentzian bands of the Drude, MIR, and DS contributions.

[1] K. Hashimoto, H. Irie, and A. Fujishima, TiO_2 photocatalysis: A historical overview and future prospects, Jpn. J. Appl. Phys. **44**, 8269 (2005).

[2] A. Fujishima and K. Honda, Electrochemical photolysis of water at a semiconductor electrode, Nature (London) **238**, 37 (1972).

[3] E. Baldini, L. Chiodo, A. Dominguez *et al.*, Strongly bound excitons in anatase TiO_2 single crystals and nanoparticles, Nat. Commun. **8**, 13 (2017).

[4] E. Baldini, T. Palmieri, E. Pomarico, G. Auböck, and M. Chergui, Clocking the ultrafast electron cooling in anatase titanium dioxide nanoparticles, ACS Photon. **5**, 1241 (2018).

[5] E. Baldini, T. Palmieri, A. Dominguez, P. Ruello, A. Rubio, and M. Chergui, Phonon-driven selective modulation of exciton oscillator strengths in anatase TiO_2 nanoparticles, Nano Lett. **18**, 5007 (2018).

[6] E. Baldini *et al.*, Exciton control in a room temperature bulk semiconductor with coherent strain pulses, Sci. Adv. **5**, eaax2937 (2019).

[7] E. Baldini, T. Palmieri, A. Dominguez, A. Rubio, and M. Chergui, Giant exciton Mott density in anatase TiO_2, Phys. Rev. Lett. **125**, 116403 (2020).

[8] B. O'Regan, and M. Grätzel, A low-cost, high-efficiency solar cell based on dye-sensitized colloidal TiO_2 films, Nature (London) **353**, 737 (1991).

[9] P. Orgiani *et al.*, Tuning the optical absorption of anatase thin films across the visible-to-near-infrared spectral region, Phys. Rev. Appl. **13**, 044011 (2020).

[10] C. Bigi *et al.*, Distinct behavior of localized and delocalized carriers in anatase TiO_2 (001) during reaction with O_2, Phys. Rev. Mater. **4**, 025801 (2020).

[11] H. Cheng and A. Selloni, Surface and subsurface oxygen vacancies in anatase TiO_2 and differences with rutile, Phys. Rev. B **79**, 092101 (2009).

[12] Y. Xiao *et al.*, A review of memristor: Material and structure design, device performance, applications and prospects, Sci. Technol. Adv. Mater. **24**, 2162323 (2023).

[13] M.-J. Lee, A fast, high-endurance and scalable non-volatile memory device made from asymmetric Ta_2O_{5-x}/TaO_{2-x} bilayer structure, Nat. Mater. **10**, 625 (2011).

[14] F. Kousar, First principles investigation of oxygen vacancies filaments in polymorphic Titania and their role in memristor's applications, Chaos, Solitons and Fractals **148**, 111024 (2021).

[15] K. Szot *et al.*, TiO_2-a prototypical memristive material, Nanotechnol. **22**, 254001 (2011).

[16] B. Magyari-Köpe, M. Tendulkar, S.-G. Park, H. D. Lee, and Y. Nishi, Resistive switching mechanisms in random access memory devices incorporating transition metal oxides: TiO_2, NiO and $Pr_{0.7}Ca_{0.3}MnO_3$, Nanotechnol. **22**, 254029 (2011).

[17] D. Emin, Optical properties of large and small polarons and bipolarons, Phys. Rev. B **48**, 13691 (1993).

[18] P. Calvani, Optical properties of polarons, Riv. Nuovo Cimento Soc. Ital. Fis. **24**, 1 (2001).

[19] X. Shan *et al.*, Plasmonic Optoelectronic Memristor Enabling Fully Light-Modulated Synaptic Plasticity for Neuromorphic Vision, Adv. Sci. **9**, 2104632 (2022).

[20] H. Li, H. Yu, X. Sun, and L. Pan, Recent advances in bioinspired vision sensor arrays based on advanced optoelectronic materials, APL Mater. **11**, 080601 (2023).

[21] D. Knez *et al.*, Unveiling oxygen vacancy superstructures in reduced anatase thin films, Nano Lett. **20**, 6444 (2020).

[22] S. Lupi *et al.*, Performance of SISSI, the infrared beamline of the ELETTRA storage ring, J. Opt. Soc. Am. B **24**, 959 (2007).

[23] M. Dressel and G. Grüner, *Electrodynamics of Solids: Optical Properties of Electrons in Matter* (Cambridge University Press, Cambridge, 2002).

[24] G. Mattioli, P. Alippi, F. Filippone, R. Caminiti, and A. A. Bonapasta, Deep versus shallow behavior of intrinsic defects in Rutile and anatase TiO_2 polymorphs, J. Phys. Chem. C **114**, 21694 (2010).

[25] P. Di Pietro *et al.*, TeraFERMI: A superradiant beamline for THz nonlinear studies at the FERMI free electron laser facility, Synchrotron Radiat. News **30**, 36 (2017).

[26] A. Perucchi *et al.*, The TeraFERMI terahertz source at the seeded FERMI free-electron-laser facility, Rev. Sci. Instr. **84**, 022702 (2013).

[27] E. Roussel *et al.*, Single-shot terahertz time-domain spectrometer using 1550 nm probe pulses and diversity electro-optic sampling, Opt. Express **31**, 31072 (2023).

[28] N. Adhlakha *et al.*, The TeraFERMI electro-optic sampling set-up for fluence-dependent spectroscopic measurements, Condens. Matter **5**, 8 (2020).

[29] M. Jewariya, M. Nagai, and K. Tanaka, Ladder climbing on the anharmonic intermolecular potential in an amino acid microcrystal via an intense monocycle terahertz pulse, Phys. Rev. Lett. **105**, 203003 (2010).

[30] P. E. Kornilovitch, Periodically driven small polarons, Phys. Rev. B **95**, 165121 (2017).

[31] S. A. Bretschneider, I. Ivanov, H. I. Wang, K. Miyata, X. Zhu, and M. Bonn, Quantifying polaron formation and charge carrier cooling in lead-iodide perovskites, Adv. Mater. **30**, 1707312 (2018).

[32] P. A. Mante, C. Stoumpos, M. Kanatzidis *et al.*, Electron–acoustic phonon coupling in single crystal $CH_3NH_3PbI_3$ perovskites revealed by coherent acoustic phonons, Nat. Commun. **8**, 14398 (2017).

[33] A. Levchuk, B. Wilk, G. Vaudel, F. Labbé, B. Arnaud, K. Balin, J. Szade, P. Ruello, and V. Juvé, Coherent acoustic phonons generated by ultrashort terahertz pulses in nanofilms of metals and topological insulators, Phys. Rev. B **101**, 180102(R) (2020).

[34] E. R. Cardozo de Oliveira *et al.*, Probing gigahertz coherent acoustic phonons in TiO_2 mesoporous thin films, Photoacoustics **30**, 100472 (2023).

[35] M. Weis, K. Balin, R. Rapacz, A. Nowak, M. Lejman, J. Szade, and P. Ruello, Ultrafast light-induced coherent optical and acoustic phonons in few quintuple layers of the topological insulator Bi_2Te_3, Phys. Rev. B **92**, 014301 (2015).

[36] Y. Ding and B. Xiao, Anisotropic elasticity, sound velocity and thermal conductivity of TiO_2 polymorphs from first principles calculations, Comput. Mater. Sci. **82**, 202 (2014).

[37] B. H. Elias, B. M. Ilyas, and N. S. Saadi, A first principle study of the perovskite lanthanum aluminate, Mater. Res. Express **5**, 086302 (2018).

[38] S. K. Chaluvadi *et al.*, Pulsed laser deposition of oxide and metallic thin films by means of Nd:YAG laser source operating at its 1st harmonics: Recent approaches and advances, J. Phys. Mater. **4**, 032001 (2021).

[39] P. Orgiani *et al.*, Dual pulsed laser deposition system for the growth of complex materials and heterostructures, Rev. Sci. Instrum. **94**, 033903 (2023).

[40] A. B. Kuzmenko, Kramers–Kronig constrained variational analysis of optical spectra, Rev. Sci. Instrum. **76**, 083108 (2005).

[41] N. Adhlakha, Z. Ebrahimpour, P. Di Pietro, J. Schmidt, F. Piccirilli, D. Fausti, A. Montanaro, E. Cappelluti, S. Lupi, and A. Perucchi, Terahertz saturable absorption from relativistic high-temperature thermodynamics in black phosphorus, Phys. Rev. Appl. **20**, 054039 (2023).